Chinese Chemical Letters 34 (2023) 107248

Contents lists available at ScienceDirect

Chinese Chemical Letters

journal homepage: www.elsevier.com/locate/cclet

In situ electrochemical dehydrogenation of ultrathin $Co(OH)_2$ nanosheets for enhanced hydrogen evolution

Qian Zhou[a], Qihang Bian[a], Liling Liao[a], Fang Yu[a,*], Dongyang Li[a], Dongsheng Tang[a,*], Haiqing Zhou[a,b,*]

[a] *Department of Physics and Synergetic Innovation Center for Quantum Effects and Applications, Key Laboratory of Low-Dimensional Quantum Structures and Quantum Control of Ministry of Education, Key Laboratory for Matter Microstructure and Function of Hunan Province, Hunan Normal University, Changsha 410081, China*

[b] *Hunan Joint International Laboratory of Advanced Materials and Technology for Clean Energy, Hunan University, Changsha 410082, China*

ARTICLE INFO

Article history:
Received 3 January 2022
Revised 23 January 2022
Accepted 17 February 2022
Available online 22 February 2022

Keywords:
Hydrogen evolution reaction
Transition metal hydroxide
In-situ electrochemical dehydrogenation
In-plane heterostructure
Water splitting

ABSTRACT

Transition metal hydroxides/oxyhydroxides have recently emerged as highly active electrocatalysts for oxygen evolution reaction in alkaline water electrolysis, while have not yet been widely investigated for hydrogen evolution electrocatalysts owing to their unfavorable H*-adsorption, making it difficult to construct an overall-water-splitting cell for hydrogen production. In this work, we proposed a straightforward and effective approach to develop an efficient in-plane heterostructured $CoOOH/Co(OH)_2$ catalyst via *in-situ* electrochemical dehydrogenation method, in which the dehydrogenated –CoOOH and $Co(OH)_2$ at the surface synergistically boost the hydrogen evolution reaction (HER) kinetics in base as confirmed by high-resolution transmission electron microscope, synchrotron X-ray absorption spectroscopy, and electron energy loss spectroscopy. Due to the *in-situ* dehydrogenation of ultrathin $Co(OH)_2$ nanosheets, the catalytic activity of the $CoOOH/Co(OH)_2$ heterostructures is progressively improved, which exhibit outstanding hydrogen-evolving activity in base requiring a low overpotential of 132 mV to afford 10 mA/cm^2 with very fast reaction kinetics after 60 h dehydrogenation. The gradually improved catalytic performance for the $CoOOH/Co(OH)_2$ is probably due to the enhanced H*-adsorption induced by the synergistic effect of heterostructures and better conductivity of CoOOH relative to electrically insulating $Co(OH)_2$. This work will open the opportunity for a new family of transition metal hydroxides/oxyhydroxides as active HER catalysts, and also highlight the importance of using in situ techniques to construct precious metal-free efficient catalysts for alkaline hydrogen evolution.

Electrocatalytic water splitting driven by renewable energies (*e.g.*, solar, wind, geothermal energy) has widely regarded as a safe and environmentally friendly pathway for hydrogen production [1–6]. At present, water splitting is more favored in alkaline electrolyte by most people due to its compatibility with inexpensive and earth-abundant electrocatalysts and cheap electrolyzer construction [7–11]. However, most noble metal-free HER catalysts (*e.g.*, transition metal sulfides [12–15], selenides [16–20], phosphides [21–26]) performing superior activity in acidic solution, possess unsatisfied HER performance in alkaline electrolytes owing to their poor capability for H_2O adsorption/dissociation. Based on this point, intensive efforts have been devoted to further improving the catalytic performance by hybridizing these materials with transition metal hydroxides (*e.g.*, $Ni(OH)_2$, $Co(OH)_2$, NiFe LDH) [27–29]. Here, transition metal hydroxides are reported to serve as OH^- (generated by H_2O electrolysis) adsorption sites rather than H*-adsorption centers, which indicates that the catalysts promoter of transition metal hydroxides alone exhibit inferior activity for HER due to the vital role of hydrogen binding in this process. In this sense, it is very promising if we can find out some useful routes to activate the reaction kinetics of transition metal hydroxides. Actually, it is interesting to note that transition metal oxyhydroxides as the intermediates in the transformation process from hydroxides to oxides have been demonstrated to be electrocatalytically active for HER [30,31]. For example, Pillai *et al.* investigated the catalytic activity of CoOOH towards HER by calculating the adsorption energy of hydrogen atom, and the

* Corresponding authors at: Department of Physics and Synergetic Innovation Center for Quantum Effects and Applications, Key Laboratory of Low-Dimensional Quantum Structures and Quantum Control of Ministry of Education, Key Laboratory for Matter Microstructure and Function of Hunan Province, Hunan Normal University, Changsha 410081, China.

E-mail addresses: fyu@hunnu.edu.cn (F. Yu), dstang@hunnu.edu.cn (D. Tang), hqzhou@hunnu.edu.cn (H. Zhou).

https://doi.org/10.1016/j.cclet.2022.02.053
1001-8417/

results suggest that CoOOH is a promising candidate for HER [31]. Therefore, as a missing piece in alkaline HER, heterostructures by integrating transition metal oxyhydroxides with hydroxides is highly expected to exhibit outstanding hydrogen-evolving activity considering better conductivity of CoOOH relative to $Co(OH)_2$.

Recently, *in-situ* electrochemical activation has drawn considerable attention as a new pretreating strategy for tuning electrocatalytic activity owing to its simplicity, variable control and flexibility [32–36]. More importantly, the electrochemical activation strategy exerted on the as-obtained precursors would *in situ* create abundant active species at the surface, always keeping a strong binding force between the active species and conductive supports, which would further facilitate the electron transfer from the electrode to the catalyst surface and ensure structural stability during the durability tests [36,37]. In addition, the local electronic structure and morphology of catalysts can be effectively modulated *via in-situ* electrochemical tuning technique [38,39]. For example, Hu *et al.* reported an *in-situ* electrochemical activation method to pretreat Ni-based ligand 1,4-benzenedithiol (Ni-BDT) nanosheets, which can be transformed into ultrathin metallic Ni (Ni^0) nanosheets with trace sulfide ($S_{ads}{}^{\delta-}$) adsorbed on the surface under a cathodic potential [37]. Benefiting from the Ni^0-$S_{ads}{}^{\delta-}$ interface, the water dissociation process has been greatly promoted, thereby significantly enhancing HER activity in an alkaline electrolyte. Besides the *in-situ* electrochemical reduction, the *in-situ* electrochemical etching also can be utilized to regulate the activity of catalysts. For instance, Hu's group adopted a galvanostatical etching method to activate the OER performance of perovskite $CoSn(OH)_6$ nanocubes *via* dissolving Sn hydroxides, creating O-vacancies and generating porous structures [38].

Inspired by the aforementioned *in-situ* strategies, we devoted to constructing porous cobalt-based in-plane oxyhydroxide/hydroxide ($CoOOH/Co(OH)_2$) heterostructures with outstanding HER activity from electrochemically inert $Co(OH)_2$ *via* an *in-situ* electrochemical dehydrogenation/activation method. The electrochemically dehydrogenated hybrid catalyst shows a superior catalytic activity toward HER with a low overpotential of 132 mV to reach 10 mA/cm^2, which is greatly decreased in comparison with that of pristine $Co(OH)_2$ (464 mV). This unusual self-optimizing performance can be derived from the generation of $CoOOH/Co(OH)_2$ heterostructures, in which $Co(OH)_2$ acts as water adsorption/dissociation promoter and CoOOH serves as H^*-adsorption site as well as the improved electrical conductivity and charge transfer of the as-obtained catalysts.

In order to fabricate an in-plane heterostructure between conductive CoOOH and $Co(OH)_2$, we employed a novel strategy called *in-situ* electrochemical activation to dehydrogenate ultrathin $Co(OH)_2$ nanosheets under a constant current density of -10 mA/cm^2 in 1.0 mol/L KOH electrolyte. The activation process was performed using a three-electrode electrochemical cell Fig. 1a illustrates the evolution of morphology and component of $Co(OH)_2$ nanosheets as efficient HER catalysts in the *in-situ* electrochemical dehydrogenation process Fig. 1b shows the X-Ray diffraction (XRD) patterns of pristine $Co(OH)_2$ and $Co(OH)_2$ after *in-situ* electrochemical dehydrogenation (under reduction current density of 10 mA/cm^2) for 60 h (denoted as: $Co(OH)_2$-60). Although tiny peaks shift induced by interlayer ions ($NO_3{}^-$ and $CO_3{}^{2-}$) can be observed, the diffraction peaks of pristine $Co(OH)_2$ located at around 18.1°, 33.0°, and 59.4° can be indexed to (001), (100) and (003) planes of hexagonal $Co(OH)_2$ (PDF #45–0031). After electrochemical dehydrogenation, the peaks also can be well maintained for $Co(OH)_2$-1 and $Co(OH)_2$-5 samples (Fig. S1 in Supporting information), while two new prominent diffraction peaks at around 19.8° and 38.7° can be observed for $Co(OH)_2$-60, which indicates that CoOOH would be gradually generated with the prolonged activation time Fig. 1c gives the typical TEM image of pristine $Co(OH)_2$, and it clearly

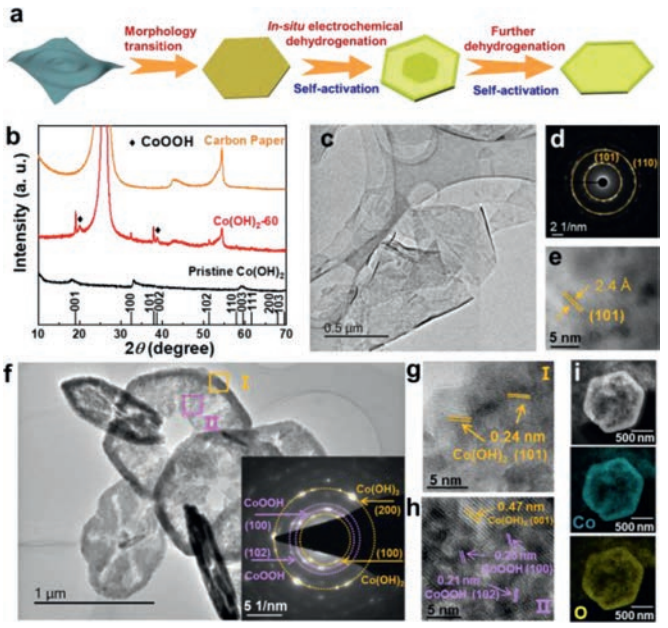

Fig. 1. (a) Schematic illustration of the *in-situ* electrochemical dehydrogenation/activation process. (b) A typical XRD pattern of pristine $Co(OH)_2$, activated $Co(OH)_2$, and carbon paper. (c) TEM image, (d) SAED pattern, (e) HRTEM image of pristine $Co(OH)_2$. (f) TEM image, (g, h) HR-TEM images selected in areas I and II, (i) STEM elemental mapping of $Co(OH)_2$–60.

shows a thin, smooth and flexible sheet-like morphology. The selected area electron diffraction (SAED) pattern shows well-defined diffractions rings, indicating the polycrystalline nature of $Co(OH)_2$ (Fig. 1d). The two rings can be ascribed to (101) and (110) lattice planes of the hexagonal $Co(OH)_2$ (space group P-3m1). As can be observed from high-resolution TEM (HRTEM) image (Fig. 1e), the lattice fringes are randomly oriented, and a lattice spacing of 0.24 nm can be attributed to (101) plane of $Co(OH)_2$, which is in good agreement with the SAED result.

The *in-situ* electrochemical dehydrogenation of $Co(OH)_2$ nanosheets was conducted at an cathodic current density of 10 mA/cm^2, and they possess different morphologies with the prolonged of time. At the early stage, the ultrathin sheets morphology gradually transforms into hexagonal nanodiscs (Fig. S2 in Supporting information). With the increase of time, the nanosheets disappear and the solid structures became core-shell nanodiscs with a rough surface (Fig. S3 in Supporting information). At last, the solid core began to disappear, showing a nanoplate or nanoring-like structure. Typically, $Co(OH)_2$-60 presents a nanoplate morphology with some pores in the centers and thicker rings around the out border (Fig. 1f). The inset of Fig. 1f is the SAED pattern of $Co(OH)_2$-60, in which the marked yellow rings can be ascribed to the (100) and (200) planes of $Co(OH)_2$, while the red rings can be assigned to the (100) and (102) planes of CoOOH, corroborating the *in situ* formation of an in-plane heterostructure between CoOOH and $Co(OH)_2$. To further verify the composition and crystal structure of the $Co(OH)_2$-60, HRTEM images in the interior and exterior areas are selected and marked by yellow and purple squares (Fig. 1f, I and II). In the area I, the lattice fringes with a distance of 0.24 nm can be clearly observed, which is corresponding to (101) plane of $Co(OH)_2$ (Fig. 1g). In area II, it not only shows the (001) plane of $Co(OH)_2$, but also displays the (100) and (102) planes of CoOOH with D-spacings of 0.25 nm and 0.21 nm (Fig. 1h), which is consistent with the SAED and XRD patterns. In addition, the STEM elemental mappings reveal the uniform distribution of Co and O in the as-prepared $Co(OH)_2$-60

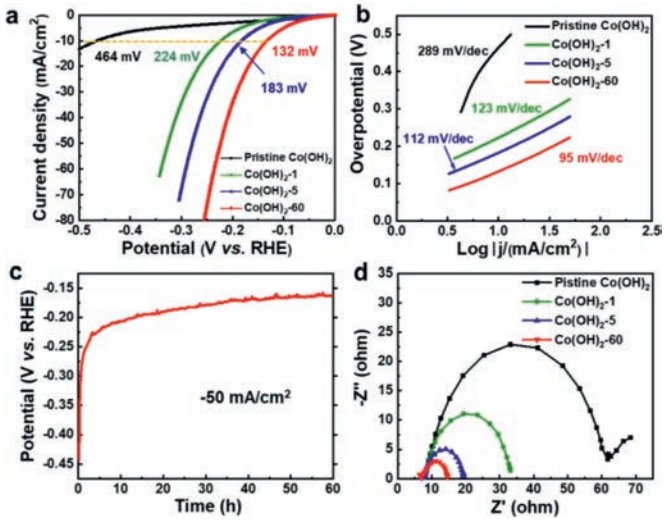

Fig. 2. (a) *iR*-Corrected polarization curves in 1.0 mol/L KOH solution of various electrocatalysts as indicated (scan rate: 5 mV/s). (b) Tafel plots derived from the polarization curves in (a). (c) Chronopotentiometry curve of $Co(OH)_2$ at a constant current density of −50 mA/cm^2. (d) Nyquist plot measured at potential of −0.2 V vs. RHE.

(Fig. 1i). All of these above observations confirm the uniform formation of CoOOH during the dehydrogenation process.

To verify the effects of heterostructures on the catalytic activity of CoOOH/$Co(OH)_2$, electrochemical measurements of pristine $Co(OH)_2$ and dehydrogenated $Co(OH)_2$ after *in-situ* activation were conducted using a standard three-electrode system in 1.0 mol/L KOH. The pristine $Co(OH)_2$ shows inferior HER performance with an overpotential of 464 mV at a current density of 10 mA/cm^2, indicating that it is a truly poor candidate for HER catalysts (Fig. 2a). However, constant cathodic current density (10 mA/cm^2) exerted on the as-prepared catalyst results in an activation and dehydrogenation process, which is evidenced by the dramatic decrease of overpotentials and gradual improvement of the catalytic activities. Specifically, the as-prepared $Co(OH)_2$-1 and $Co(OH)_2$-5 require overpotentials of 224 mV and 183 mV to reach a current density of 10 mA/cm^2, respectively. In particular, $Co(OH)_2$-60 displays very superior electrocatalytic activity with an overpotential of only 132 mV at 10 mA/cm^2. A similar electrochemical performance improvement can be observed under continuous cyclic voltammetry between potentials of 0 and −0.3 V vs. RHE at a scan rate of 20 mV/s. After 1000 CV cycles, a low overpotential of only 256 mV is required for activated $Co(OH)_2$, which is 210 mV lower than that of pristine $Co(OH)_2$ (Fig. S4 in Supporting information). The CoOOH/$Co(OH)_2$ heterostructures were *in-situ* generated during the process of continuous cyclic voltammetry measurement, as shown in (Fig. S5 Supporting information), in which two obvious diffraction peaks are detected belonging to CoOOH, suggesting the repeatable and credible dehydrogenation of $Co(OH)_2$ to CoOOH at the surface for efficient HER catalysis. To exclude that the enhanced performance of the heterostructured catalyst is only originated from the increasement of CoOOH, electrochemical measurement has been conducted on pure CoOOH. As exhibited in (Fig. S6a Supporting information), the pure CoOOH requires overpotential of 453 mV to reach a current density of 10 mA/cm^2, which is much higher than those of activated catalysts ($Co(OH)_2$-1, $Co(OH)_2$-5, and $Co(OH)_2$-60). Moreover, the pure CoOOH shows sluggish catalytic kinetics as evidenced by the large Tafel slope of 159 mV/dec (Fig. S6b in Supporting information). This result reveals that pure CoOOH shows inferior HER performance and also demonstrates that the superior alkaline HER activity for the CoOOH/$Co(OH)_2$ can be ascribed to the synergistic effect between the two components rather than the increase of CoOOH. The accelerated electrocatalytic kinetics of $Co(OH)_2$ during the activation process is also evidenced by the distinct reduced Tafel slope, as exhibited in Fig. 2b. The Tafel slope of $Co(OH)_2$-60 is 95 mV/dec, which is much lower than that of pristine $Co(OH)_2$ (289 mV/dec). Although transition metal (oxy)hydroxides alone have been regarded as unqualified candidates for HER, our optimized $Co(OH)_2$-based catalyst after *in-situ* electrochemical activation forming heterostructured CoOOH/$Co(OH)_2$ exhibits superb catalytic activity, which outperforms most of the reported transition metal (oxy)hydroxides-based electrocatalysts tested under similar conditions (Table S1 in Supporting information), such as $Ni(OH)_2/MoS_2$ [40], $Ni(OH)_2/NiCo_2O_4$ [41], $CeO_2/Co(OH)_2$ [42] and $Co(OH)_2$@P-NiCo-LDH [43], and is even comparable to those of cobalt-based catalysts with much higher conductivity including phosphides (CoP@FeCoP and CoP@NC/graphene) [44,45], selenides (p-$CoSe_2$/CC and $(Ni,Co)_{0.85}Se$) [46,47], nitrides ($NiCo_2N$/NF and Co_3N) [48,49], and sulfides (Co_9S_8 and CoS_x/Ni_3S_2@NF) [50,51]. The *in-situ* activation process can also be observed in the chronopotentiometry test conducted at a larger current density of −50 mA/cm^2 (Fig. 2c), showing that the potential increases rapidly in the initial 5 h, and then increases gradually until the 60 h, which is consistent with the variation of the polarization curves in Fig. 2a. In addition, electrochemical impedance spectroscopy (EIS) was employed to explore the charge-transfer kinetics during the activation process. As presented in Fig. 2d, charge-transfer resistance of $Co(OH)_2$ is continuously reduced from 56 Ω to 9 Ω with the increase of activation time, suggesting that *in-situ* electrochemical activation could efficiently improve the conductivity of the heterostructure, and accelerate the charge transfer kinetics between the electrolyte and catalysts.

In order to gain an in-depth understanding of the mechanism behind this electrochemical dehydrogenation/activation process, we conducted a series of measurements including synchrotron X-ray absorption spectroscopy (XAS) and electron energy loss spectroscopy (EELS). The soft XAS can provide the useful information of electronic structure of Co in our as-prepared catalysts, as shown in Fig. 3a. Apparently, the L_3 peaks located at 776.8, 778.1, 778.6, and 779.5 eV can be assigned to Co^{2+} in pristine $Co(OH)_2$ [52]. While a peak located at 780.1 eV appears with the increase of activation time, which can be ascribed to Co^{3+} [52,53]. It is clearly seen that the intensity of this peak increases with the prolonged activation time, suggesting the rising ratio of Co^{3+}. In addition, X-ray absorption near-edge structure (XANES) spectra at the Co K-edge also demonstrate the existence of Co^{3+}. As shown in Fig. 3b, the absorption edge is shifted to higher energy from the pristine $Co(OH)_2$ to $Co(OH)_2$-60, along with a broadening of the white line peak, revealing a distinct increase of the Co oxidation state. Although the XAS results suggest the presence of Co^{3+}, it cannot probe the dynamic electronic structure of the catalyst during the electrocatalytic reaction. Therefore, *in-situ* Raman spectroscopy was conducted to directly monitor the structural transformation of $Co(OH)_2$ under the electrochemical activation conditions. Fig. 3c shows Raman spectra of pristine $Co(OH)_2$ and $Co(OH)_2$ at selected activation time operated at cathodic current density of 10 mA/cm^2 immersed in 1.0 mol/L KOH. Apparently, the bands located at 455 and 515 cm^{-1} can be assigned to the Co–O symmetric stretching mode (A_g) and O–Co–O bending mode derived from the $Co(OH)_2$ nanosheets [54]. After 1 h activation, the bands of $Co(OH)_2$ are retained and no band-shift or new bands can be observed. When the electrochemical activation time increases to 5 h, one new prominent band appears at around 688 cm^{-1} besides the band of $Co(OH)_2$, which is ascribed to CoOOH [55,56]. With prolonged activation time, the bands of $Co(OH)_2$ gradually disappear. When the activation time increases to 60 h, bands of $Co(OH)_2$ disappear and bands appearing at 497 cm^{-1} belongs to the CoOOH

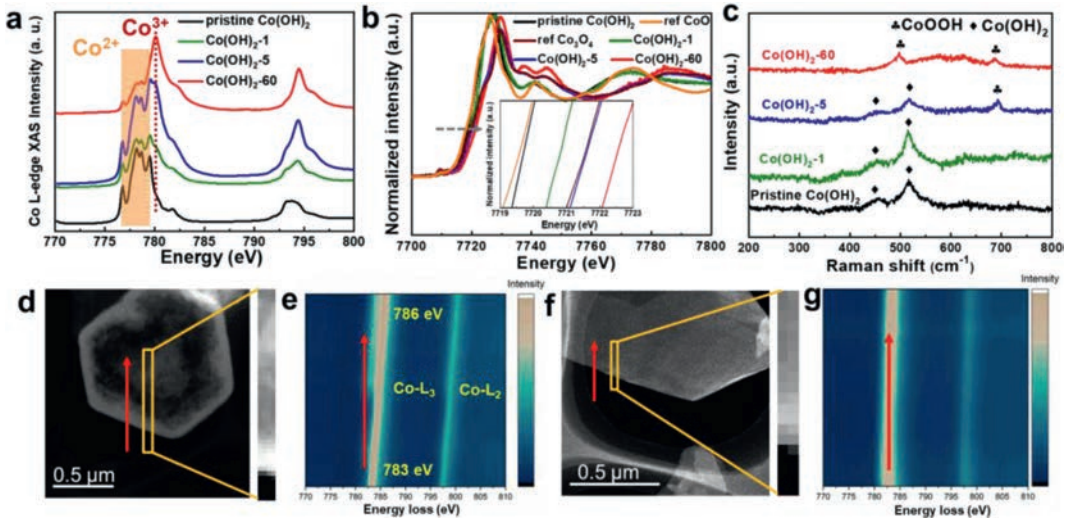

Fig. 3. (a) Co L-edge XAS and (b) Co K-edge XANES spectra of the pristine $Co(OH)_2$ and $Co(OH)_2$ after electrochemical activation. (c) *in-situ* Raman spectrum of $Co(OH)_2$ under different activation stages. (d) Dark-field STEM image and (e) corresponding EELS mapping of $Co(OH)_2$-60. (f) Dark-field STEM image and (g) corresponding EELS mapping of pristine $Co(OH)_2$.

[54], indicating the *in-situ* formation of CoOOH under cathodic current operation, which is consistence with the *ex-situ* XAS result. To precisely investigate the distribution of CoOOH on the nanoplates, EELS mappings of pristine $Co(OH)_2$ and $Co(OH)_2$-60 were acquired from the edge to the interior of the nanoplates, as shown in Figs. 3d-g. Unlike the pristine $Co(OH)_2$ that no obvious shift of L_3 and L_2 peaks can be detected, L_3 and L_2 peaks of $Co(OH)_2$-60 gradually shift to higher energy losses from the border to the inner of the nanoplates, indicating that the percentage of the Co^{3+} (CoOOH) increases gradually from the exterior to the interior of the $Co(OH)_2$-60 nanoplates, which is consistent with the HRTEM observations.

Based on the above characterizations, the evolution of morphology with electrochemical activation time for $Co(OH)_2$ can be assigned to the combination of recrystallization and inside-out Ostwald ripening mechanism. Firstly, the pristine $Co(OH)_2$ featuring ultrathin nanosheets morphology would gradually convert to nanoplates-like $Co(OH)_2$ *via* the recrystallization in an alkaline electrolyte [57]. As time goes on, the particles on the edges are easy to grow into large ones, because the recrystallization preferentially occurs at the solid-liquid interface, while the inner crystallites tend to dissolve owing to the loose packing [58]. Therefore, the core-shell like morphology would gradually form on the nanosheet owing to the growth of exterior part and consumption of the inner substances. With prolonged time, the solid core gradually evacuates and generates some pores in the center. As the HER reaction proceeding, the surface of $Co(OH)_2$ would lose some H atoms and electrons and transform into CoOOH owing to the existence of dissolved oxygen in the electrolyte and strong concentration of OH^- near the catalysts [59]. However, the edges of the nanoplates are difficult to lose electron under reductive current because the edges are always the active sites for HER. Therefore, the center of the nanoplates tend to lose electrons, thereby generating $CoOOH/Co(OH)_2$ heterostructures. Consequently, the XAS and EELS results indicate that the as-prepared $Co(OH)_2$ nanosheets experience distinct electronic structure reconstruction under realistic catalytic conditions forming heterostructured $CoOOH/Co(OH)_2$, which is responsible for the *in-situ* electrochemical activation of $Co(OH)_2$ for HER.

As has been reported, the adsorption/dissociation of H_2O, which is regarded as a rate-limiting step in alkaline hydrogen evolution, prefers to proceed on the surfaces of transition metal hydroxides. Besides, CoOOH could serve as a more favorable site for hydrogen adsorption based on a small adsorption barrier of −0.45 eV [31]. Therefore, the superior alkaline HER activity for the $CoOOH/Co(OH)_2$ is derived from the interface engineering. As shown in Fig. 4, the $Co(OH)_2$ acts as a promoter for water adsorption and dissociation, while the produced hydrogen intermediates absorb on adjacent CoOOH and subsequently combine to give hydrogen gas. In this way, the $CoOOH/Co(OH)_2$ heterostructures effectively reduce the energy barrier of the water dissociation and accelerates the alkaline HER process accordingly.

In this work, $CoOOH/Co(OH)_2$ heterostructures have been designed and fabricated as an efficient alkaline HER electrocatalyst *via in-situ* electrochemical dehydrogenation strategy. The resultant $CoOOH/Co(OH)_2$ heterostructures exhibit significantly enhanced HER performance with a small overpotential of 132 mV to afford 10 mA/cm^2, which is 332 mV lower than that of pristine $Co(OH)_2$. The excellent activity is probably attributed to the synergetic cooperation between $Co(OH)_2$ and CoOOH, in which $Co(OH)_2$ acts as H_2O adsorption/dissociation promoter, and CoOOH serves as H^* acceptor. We believe that our findings would provide novel insight into engineering heterostructured catalysts with outstanding HER performance in alkaline media.

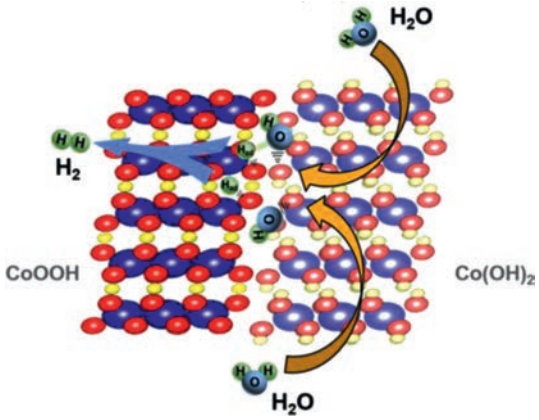

Fig. 4. Illustration of the HER mechanism on $CoOOH/Co(OH)_2$ heterostructures in alkaline solution.

Declaration of competing interest

The authors declare that they have no known competing financial interests or personal relationships that could have appeared to influence the work reported in this paper.

Acknowledgments

This project is mainly funded by National Science Foundation of China (Nos. 12074116 and 52172197), the Youth 1000 Talent Program of China, Undergraduate Scientific Research Innovation Project of China (No. 202110542037), Science and Technology Innovation Platform (No. 2019RS1032), Major Program of Natural Science Foundation of Hunan Province of Hunan Province, and Hunan Normal University (Nos. 2021133, 21CSZ004 and 21CSZ029). H. Zhou also acknowledges the support from Hunan Joint International Laboratory of Advanced Materials and Technology for Clean Energy (No. 2020CB1007). Q. Zhou acknowledges the support from Science and Technology Innovation Program of Hunan Province (No. 2021RC2075).

Supplementary materials

Supplementary material associated with this article can be found, in the online version, at doi:10.1016/j.cclet.2022.02.053.

References

[1] Y. Zhang, Q. Zhou, J.X. Zhu, et al., Adv. Funct. Mater. 27 (2017) 1702317.
[2] F. Yu, L. Yu, I.K. Mishra, et al., Mater. Today Phys. 7 (2018) 121–138.
[3] H.Y. Jin, C.X. Guo, X. Liu, et al., Chem. Rev. 118 (2018) 6337–6408.
[4] X.H. Chen, Q. Zhang, L.L. Wu, et al., Mater. Today Phys. 15 (2020) 100268.
[5] S.R. Xu, H.T. Zhao, T.S. Li, et al., J. Mater. Chem. A 8 (2020) 19729–19745.
[6] Q. Zhou, G.Q. Zhao, K. Rui, et al., Nanoscale 11 (2019) 717–724.
[7] J.X. Chen, Q.W. Long, K. Xiao, et al., Sci. Bull. 66 (2021) 1063–1072.
[8] Y. Yang, Y.M. Qian, H.J. Li, et al., Sci. Adv. 6 (2020) eaba6586.
[9] L.L. Liao, J.Y. Sun, D.Y. Li, et al., Small 16 (2020) 1906629.
[10] F.M. Cai, L.L. Liao, Y. Zhao, et al., J. Mater. Chem. A 9 (2021) 10199–10207.
[11] P.Q. Yin, G. Wu, X.Q. Wang, et al., Nano Res. 14 (2021) 4783–4788.
[12] M.R. Gao, J.X. Liang, Y.R. Zheng, et al., Nat. Commun. 6 (2015) 5982.
[13] T. Guo, L.N. Wang, S. Sun, et al., Chin. Chem. Lett. 3 (2019) 1253–1260.
[14] J.Y. Sun, F. Tian, F. Yu, et al., ACS Catal. 10 (2020) 1511–1519.
[15] Y. Yang, Y.T. Wang, H.L. He, et al., ACS Nano 14 (2020) 4925–4937.
[16] F.M. Wang, Y.C. Li, T.A. Shifa, et al., Angew. Chem. Int. Ed. 55 (2016) 6919–6924.
[17] Y. Yin, Y.M. Zhang, T.L. Gao, et al., Adv. Mater. 29 (2017) 1700311.
[18] L.L. Liao, C. Cheng, H.Q. Zhou, et al., Mater. Today Phys. 22 (2022) 100589.
[19] X.F. Yang, W. Liu, C.H. Han, et al., Mater. Today Phys. 15 (2020) 100261.
[20] G.J. Wei, K. Du, X.X. Zhao, et al., Chin. Chem. Lett. 31 (2020) 2641–2644.
[21] X. Xiao, X. Wang, B. Li, et al., Mater. Today Phys. 12 (2020) 100182.
[22] J.Y. Cai, Y. Song, Y.P. Zang, et al., Sci. Adv. 6 (2020) eaaw8113.
[23] Z.H. Pu, T.T. Liu, I.S. Amiinu, et al., Adv. Funct. Mater. 30 (2020) 2004009.
[24] D.Y. Li, L.L. Liao, H.Q. Zhou, et al., Mater. Today Phys. 16 (2021) 100314.
[25] Y. Liu, Q.G. Feng, W. Liu, et al., Nano Energy 81 (2021) 105641.
[26] Q. Zhou, L.L. Liao, Q.H. Bian, et al., Small 18 (2022) 2105642.
[27] Y.T. Luo, X. Li, X.K. Cai, et al., ACS Nano 12 (2018) 4565–4573.
[28] B. Zhang, J. Liu, J.S. Wang, et al., Nano Energy 37 (2017) 74–80.
[29] J. Hu, C.X. Zhang, L. Jiang, et al., Joule 1 (2017) 383–393.
[30] S. He, Y.Y. Huang, J.H. Huang, et al., J. Phys. Chem. C 119 (2015) 26362–26366.
[31] S.B. Pillai, B.A. Baraiya, D. Upadhyay, V. Mankad, P.K. Jha, Int. J. Hydrog. Energy 45 (2020) 23900–23907.
[32] Y. Kim, D.H.K. Jackson, D. Lee, et al., Adv. Funct. Mater. 27 (2017) 1701825.
[33] J.C. McGlynn, T. Dankwort, L. Kienle, et al., Nat. Commun. 10 (2019) 5336.
[34] Q. Li, Z.C. Xing, D.W. Wang, X.P. Sun, X.R. Yang, ACS Catal. 6 (2016) 2797–2801.
[35] T.Y. Wang, K.Z. Du, W.L. Liu, et al., J. Mater. Chem. A 3 (2015) 4368–4373.
[36] X. Shang, B. Dong, Y.M. Chai, C.G. Liu, Sci. Bull. 63 (2018) 853–876.
[37] C.Y. Hu, Q.Y. Ma, S.F. Hung, et al., Chemistry 3 (2017) 122–133.
[38] F. Song, K. Schenk, X.L. Hu, Energy Environ. Sci. 9 (2016) 473–477.
[39] M.R. Gao, M.K.Y. Chan, Y.G. Sun, Nat. Commun. 6 (2015) 7493.
[40] G.Q. Zhao, Y. Lin, K. Rui, et al., Nanoscale 10 (2018) 19074–19081.
[41] Y. Sang, X. Cao, L.X. Wang, et al., Int. J. Hydrog. Energy 45 (2020) 30601–30610.
[42] M.C. Sung, G.H. Lee, D.W. Kim, J. Alloys Compd. 800 (2019) 450–455.
[43] N. Song, S.H. Hong, M.Y. Xiao, et al., J. Colloid Interface Sci. 582 (2021) 535–542.
[44] J.H. Shi, F. Qiu, W.B. Yuan, M.M. Guo, Z.H. Lu, Chem. Eng. J. 403 (2021) 126312.
[45] M.M. Guo, F. Qiu, Y.X. Yuan, et al., Inorg. Chem. 60 (2021) 16761–16768.
[46] S. Wan, W.Y. Jin, X.L. Guo, et al., ACS Sustain. Chem. Eng. 6 (2018) 15374–15382.
[47] K.M. Xiao, L. Zhou, M.F. Shao, M. Wei, J. Mater. Chem. A 6 (2018) 7585–7591.
[48] Y.Q. Wang, B.H. Zhang, W. Pan, H.Y. Ma, J.T. Zhang, ChemSusChem 10 (2017) 4170–4177.
[49] X.Y. Ma, W. Zhang, Y.D. Deng, et al., Nanoscale 10 (2018) 4816–4824.
[50] C.Y. Zhang, S. Bhoyate, P.K. Kahol, et al., ChemNanoMat 4 (2018) 1240–1246.
[51] S. Shit, S. Chhetri, W. Jang, et al., ACS Appl. Mater. Interfaces 10 (2018) 27712–27722.
[52] A.M. Hibberd, H.Q. Doan, E.N. Glass, et al., J. Phys. Chem. C 119 (2015) 4173–4179.
[53] B. Zhang, X.L. Zheng, O. Voznyy, et al., Science 352 (2016) 333–337.
[54] J. Yang, H.W. Liu, W.N. Martens, R.L. Frost, J. Phys. Chem. C 114 (2010) 111–119.
[55] L.M. Alrehaily, J.M. Joseph, J.C. Wren, Phys. Chem. Chem. Phys. 17 (2015) 24138–24150.
[56] C.A. Triana, R. Moré, A.J. Bloomfield, et al., Matter 1 (2019) 1354–1369.
[57] K. Ding, X. Zhang, J.P. Li, P. Yang, X. Cheng, CrystEngComm 19 (2017) 5780–5786.
[58] F.Y. Kong, M. Li, X.Y. Yao, et al., CrystEngComm 14 (2012) 3858–3861.
[59] K. Kongsawatvoragul, S. Kalasina, P. Kidkhunthod, M. Sawangphruk, Electrochim. Acta 324 (2019) 134854.